

# UTE Imaging in the Musculoskeletal System

## CME

Eric Y. Chang, MD,<sup>1,2\*</sup> Jiang Du, PhD,<sup>2</sup> and Christine B. Chung, MD<sup>1,2</sup>

This article is accredited as a journal-based CME activity. If you wish to receive credit for this activity, please refer to the website: [www.wileyhealthlearning.com/jmri](http://www.wileyhealthlearning.com/jmri)

### ACCREDITATION AND DESIGNATION STATEMENT

Blackwell Futura Media Services designates this journal based CME activity for a maximum of 1 *AMA PRA Category 1 Credit*<sup>™</sup>. Physicians should only claim credit commensurate with the extent of their participation in the activity.

Blackwell Futura Media Services is accredited by the Accreditation Council for Continuing Medical Education to provide continuing medical education for physicians.

### EDUCATIONAL OBJECTIVES

Upon completion of this educational activity, participants will be better able to:

1. recognize the principles behind imaging of short T2\* tissues
2. identify ultrashort echo time (UTE) techniques in the musculoskeletal system

### ACTIVITY DISCLOSURES

No commercial support has been accepted related to the development or publication of this activity.

### Faculty Disclosures:

Editor-in-Chief: Mark E. Schweitzer, MD, has no relevant financial relationships to disclose.

CME Editor: Scott B. Reeder, MD, PhD, discloses personal stock in Cellerar Biosciences and Neuwave Medical.

### CME Committee:

Shreyas Vasanaawala, MD, PhD, discloses research support from General Electric, and founder's equity in Morpheus Medical.

Scott K. Nagle, MD, PhD, discloses consulting fees from Vertex Pharmaceuticals for consulting in design of cystic fibrosis clinical trials involving imaging; and departmental research support from General Electric for evaluation of products and development.

Mustafa R. Bashir, MD, discloses research support from Siemens Healthcare and Bayer Healthcare.

Tim Leiner, MD, PhD, discloses research support grant funding from Bracco, S.p.A., Philips Healthcare, and Bayer Healthcare.

Bonnie Joe, MD, PhD, has no relevant financial relationships to disclose.

**Authors:** Christine B. Chung, MD, Eric Y. Chang, MD, and Jiang Du, PhD have no relevant financial relationships to disclose.

This manuscript underwent peer review in line with the standards of editorial integrity and publication ethics maintained by *Journal of Magnetic Resonance Imaging*. The peer reviewers have no relevant financial relationships. The peer review process for *Journal of Magnetic Resonance Imaging* is double-blinded. As such, the identities of the reviewers are not disclosed in line with the standard accepted practices of medical journal peer review.

Conflicts of interest have been identified and resolved in accordance with Blackwell Futura Media Services' Policy on Activity Disclosure and Conflict of Interest.

### INSTRUCTIONS ON RECEIVING CREDIT

For information on applicability and acceptance of CME credit for this activity, please consult your professional licensing board.

This activity is designed to be completed within an hour; physicians should claim only those credits that reflect the time actually spent in the activity. To successfully earn credit, participants must complete the activity during the valid credit period.

Follow these steps to earn credit:

- Log on to [www.wileyhealthlearning.com/jmri](http://www.wileyhealthlearning.com/jmri)
- Read the target audience, educational objectives, and activity disclosures.
- Read the article in print or online format.
- Reflect on the article.
- Access the CME Exam, and choose the best answer to each question.
- Complete the required evaluation component of the activity.

This activity will be available for CME credit for twelve months following its publication date. At that time, it will be reviewed and potentially updated and extended for an additional period.

<sup>1</sup>Department of Radiology, VA San Diego Healthcare System, San Diego, California, USA.

<sup>2</sup>Department of Radiology, University of California, San Diego Medical Center, San Diego, California, USA.

Contract grant sponsor: VA Clinical Science Research and Development Service; Contract grant numbers: Career Development Grant 11K2CX000749 and Merit Award I01CX000625; Contract grant sponsor: National Institutes of Health (NIH); Contract grant numbers: R01DE022068 and R21 AR063894.

\*Address reprint requests to: E.Y.C., VA San Diego Healthcare System, San Diego, CA 92161. E-mail: [ericchangmd@gmail.com](mailto:ericchangmd@gmail.com)

Received June 16, 2014; Accepted July 3, 2014.

DOI 10.1002/jmri.24713

View this article online at [wileyonlinelibrary.com](http://wileyonlinelibrary.com).

Tissues, such as bone, tendon, and ligaments, contain a high fraction of components with "short" and "ultrashort" transverse relaxation times and therefore have short mean transverse relaxation times. With conventional magnetic resonance imaging (MRI) sequences that employ relatively long echo times (TEs), there is no opportunity to encode the decaying signal of short and ultrashort  $T_2/T_2^*$  tissues before it has reached zero or near zero. The clinically compatible ultrashort TE (UTE) sequence has been increasingly used to study the musculoskeletal system. This article reviews the UTE sequence as well as various modifications that have been implemented since its introduction. These modifications have been used to improve efficiency or contrast as well as provide quantitative analysis. This article reviews several clinical musculoskeletal applications of UTE.

**Key Words:** ultrashort TE; musculoskeletal tissues; quantitative MRI; bicomponent analysis

**J. Magn. Reson. Imaging 2015;41:870–883.**  
© 2014 Wiley Periodicals, Inc.

ALL BIOLOGICAL TISSUES are heterogeneous and contain a combination of components, each with an individual transverse relaxation time ( $T_2$  and  $T_2^*$ ). The observed signal intensity of a tissue at the time of magnetic resonance imaging (MRI) depends on many variables, including the mean transverse relaxation time of the components within a voxel. One commonly used classification scheme defines transverse relaxation values less than 0.1 msec as "supershort," 0.1–1 msec as "ultrashort," 1–10 msec as "short," and greater than 10 msec as "long" (1). Some tissues of the musculoskeletal system contain a high fraction of components with long transverse relaxation times, such as cartilage, and therefore have long mean transverse relaxation times. Other tissues, such as bone, tendon, and ligaments, contain a high fraction of components with "short" and "ultrashort" transverse relaxation times and therefore have short mean transverse relaxation times.

With conventional MRI sequences that employ relatively long echo times (TEs), there is limited opportunity to encode the decaying signal of short and ultrashort  $T_2/T_2^*$  tissues before it has reached zero or near zero. Although there remains clinical value with seeing the outline of the short  $T_2/T_2^*$  tissues, such as hypointense tendon outlined by hyperintense fat, a significant amount of information is lost by not being able to directly view the tissue and its internal structure (Fig. 1). Furthermore, there is no possibility of quantification, such as measuring longitudinal ( $T_1$ ) or transverse ( $T_2$  or  $T_2^*$ ) relaxation times.

A family of clinically compatible sequences is capable of providing TE values less than 1 msec (1). These can be collectively referred to as the ultrashort TE (UTE) group of sequences, although zero TE (ZTE) is also a member of this family. Since their introduction (2), UTE sequences have been employed on clinical MR systems from every major manufacturer and have

been increasingly used to study the musculoskeletal system. With UTE, TEs as short as 8  $\mu$ s (0.008 msec) have been achieved, although TE values ranging from 20–100  $\mu$ s are more typical.

Images acquired with UTE sequences can be used for qualitative evaluation, such as for alteration of the calcified layer of articular cartilage or tendon ultrastructure. Alternatively, UTE sequences can allow for quantitative evaluation, such as evaluation of the bicomponent fraction of tendon. Furthermore, preparatory pulses can be combined with UTE to sensitize the sequence to particular proton pools, such as for the evaluation of the slow molecular interactions between water and proteoglycans ( $T_{1\rho}$ ) (3).

This article reviews the UTE sequence as well as various modifications that have been implemented since its introduction. These modifications have been used to improve efficiency or contrast as well as provide quantitative analysis. We also review select clinical musculoskeletal applications of UTE. This review will only focus on proton imaging, although UTE sequences can be useful for imaging of other nuclei including phosphorus or sodium.

## UTE TECHNIQUES

Conventional echo-forming sequences, such as RARE (rapid acquisition with relaxation enhancement, also known as fast spin echo) and gradient-recalled echo (GRE), cannot be used to generate echo times less than 1 msec on clinical systems. Using these sequences, the majority of signal from short components has decayed prior to echo formation. In fact, significant transverse relaxation can occur even during radiofrequency (RF) pulse excitation.

The UTE sequence uses a short RF pulse and acquires data as soon as possible after excitation finishes. Data acquisition occurs while the readout gradient is being ramped on (Fig. 2). The sampling pattern of  $k$ -space is radial, filled from the center out, and is nonlinear in time (4). Slice-selection with 2D imaging is achieved with two excitations, each half of a conventional slice selection pulse. The first pulse uses a positive gradient and the second a negative gradient, together resulting in the same scenario as a single complete excitation pulse (2). Half pulses can also be used for volumetric imaging with a variety of methods, each with challenges and proposed solutions (5). Alternatively, 3D imaging can be achieved with a nonselective (hard) excitation pulse followed by a 3D radial acquisition (4). Judicious use and placement of coils allows for signal to originate mainly from the structures of interest. For instance, the use of a surface coil can allow small field-of-view imaging of a superficial anatomic structure without aliasing from deeper structures that are not of interest.

One of the limitations of radial acquisition is that many more acquisitions are required to satisfy the Nyquist criterion compared with rectangular (Cartesian) sampling. To improve overall efficiency, a number of modifications have been proposed to fill

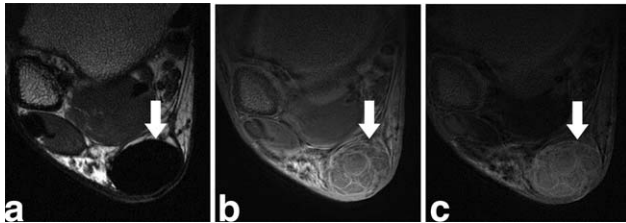


**Figure 1.** Axial images of an asymptomatic volunteer after Achilles tendon repair. Proton density fast spin echo (FSE) image using 6.6 msec TE (a) shows no signal within the Achilles tendon (arrow). 3D-UTE-Cones image using 30  $\mu$ s TE (b) shows internal structure of the repaired Achilles tendon. 30  $\mu$ s minus 6.6 msec subtraction image (c) highlights short  $T_2^*$  components, which are more abundant between healed fascicles. Images courtesy of Michael Carl, PhD.

$k$ -space, including twisted, spiral, and cones projection methods (6,7). Other UTE-type sequences that have been used to image species with ultrashort transverse relaxation times include the acquisition-weighted stack of spirals (AWSOS) and variable TE (vTE) sequences. The AWSOS sequence uses selective excitation, variable-duration slice encoding, and mobile spiral readout to sample a cylindrical volume in  $k$ -space (8). The vTE sequence uses Cartesian  $k$ -space sampling, but TE is shortened with asymmetric RF pulses, partial echoes, and ramp sampling (9). Although all of these methods result in improved overall efficiency compared with radial acquisition, usually longer readout durations are required and blurring may result.

An alternative approach to imaging of tissues with short transverse relaxation is the application of the readout gradient prior to excitation. The RF pulse that is applied can be a short, hard pulse, referred to as the zero echo time (ZTE) technique (10) or can be a longer, frequency-modulated pulse with interleaved transmit-receive operation, known as sweep imaging with Fourier transformation (SWIFT) (11). The elimination of rapidly switching gradients between TR intervals has many benefits, including decreased acoustic noise and reduced eddy current effects. These sequences are inherently 3D due to the pres-

ence of the readout gradient, which prevents simultaneous application of a slice selection gradient in another direction (10). The dead time that is caused by the finite duration of the RF pulse, transmit-receive switching, and digital bandpass filtering results in a gap of data at the center of  $k$ -space (10). The missing data challenge can be addressed with acquisition oversampling and algebraic reconstruction in the ZTE technique (10) or filled with a Cartesian single-point imaging technique, known as pointwise encoding time reduction with radial acquisition (PETRA) (12). A limitation of these techniques is less versatile contrast manipulation, although inversion preparation pulses can create  $T_1$  contrast (13,14).

### Qualitative Imaging for Morphologic or Anatomic Analysis

With the UTE technique, it is possible to obtain signal from tissues with short and ultrashort mean transverse relaxation times. However, images are largely proton-density-weighted and contrast between adjacent musculoskeletal structures is often not as dramatic as with conventional images. This highlights the need for manipulation of signal to optimally evaluate tissues and tissue components with rapid transverse relaxation.

Image contrast can be manipulated with appropriate selection of TE, where longer TEs add  $T_2^*$  weighting. Sequences that lack a refocusing pulse are sensitive to both macroscopic and microscopic susceptibility effects ( $T_2^*$ ), although use of ultrashort TEs minimizes dephasing. Another basic method is with image subtraction between a UTE image and a second gradient echo image with much longer TE. The UTE image will capture signals from both long and short  $T_2^*$  components, whereas the longer TE image will capture signal from the long  $T_2^*$  components. Subtraction of the two images will result in selective display of short  $T_2^*$  components (Fig. 1). Rescaling of the UTE image prior to subtraction can be performed to decrease the signal from muscle and fat relative to the unscaled longer TE image, resulting

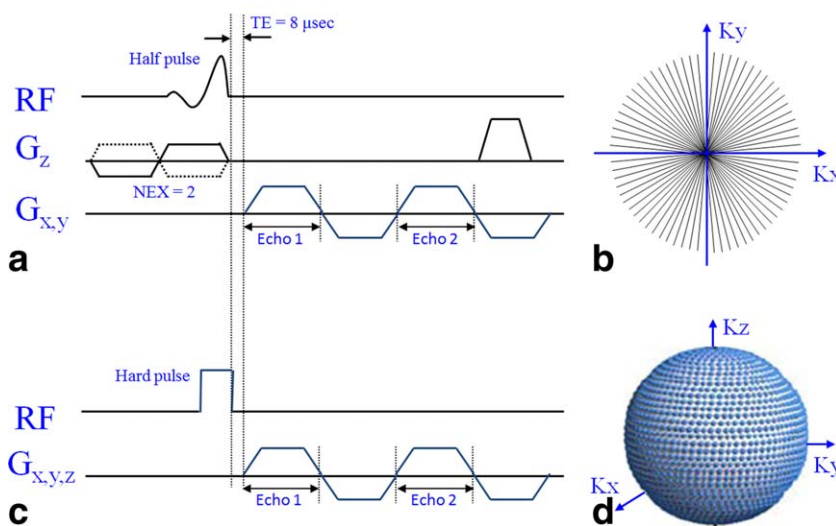


**Figure 2.** Ultrashort TE (UTE) pulse sequence diagrams and  $k$ -space trajectories. 2D-UTE sequence uses a slice-selective half-pulse excitation followed by ramp sampling (a) to fill  $k$ -space (b). 3D-UTE sequence uses a short rectangular hard pulse excitation followed by ramp sampling (c) to fill  $k$ -space (d).

in increased contrast of the short  $T_2^*$  components (15). Subtraction techniques are sensitive to patient in-plane and through-plane motion between source images.

Preparation pulses prior to UTE acquisition can introduce additional forms of contrast.  $T_1$ -weighting can be performed with saturation recovery, where a short rectangular, nonselective  $90^\circ$  pulse (e.g.,  $256 \mu\text{s}$  in duration) is delivered followed by a larger crusher gradient (16). Longitudinal magnetizations of both short and long  $T_2^*$  species are saturated and more rapid longitudinal recovery of short  $T_1$  components allows for  $T_1$ -weighting (Fig. 3).

Preparation pulses can also be used to suppress long  $T_2^*$  species, such as with long  $T_2^*$  saturation or inversion and signal nulling (17). Long  $T_2^*$  saturation techniques use a long  $90$ – $110^\circ$  RF pulse followed by a large crusher gradient (17,18). The short  $T_2^*$  components are then selectively detected with the UTE sequence since they experienced significant transverse relaxation during the long RF preparation pulse and were able to significantly recover their longitudinal magnetization. Two consecutive saturation pulses and subsequent spoiling gradients can be used for combined water- and fat-suppression, known as water- and fat-suppressed projection imaging (WASPI) (17). A limitation of saturation techniques that use hard RF pulses is that they are more sensitive to  $B_0$  and  $B_1$  inhomogeneities compared with the adiabatic inversion and signal nulling techniques. Long  $T_2^*$  inversion with adiabatic  $180^\circ$  pulses have been used to overcome this limitation (16). Similar to the long  $T_2^*$  saturation technique, the short  $T_2^*$  components are not inverted, but partially saturated during the long  $T_2^*$  inversion process. After an appropriate inversion time, the long  $T_2^*$  signals are nulled and only the short  $T_2^*$  signals are detected with the UTE sequence. A single inversion pulse can be used to reduce  $\sim 80\%$  of the signal of both fat and long- $T_2^*$  components (such as muscle) (16) or dual inversion pulses can be used for complete nulling of both (19,20).

Off-resonance saturation with subtraction can also provide contrast for the short  $T_2^*$  components (21). This technique relies on the fact that short  $T_2^*$  components have broad spectral linewidths compared with long  $T_2^*$  components such as fat and water. A high power saturation pulse placed  $+1$  to  $+2$  kHz away from the water peak results in suppression of the

short  $T_2^*$  components. Subtraction of two UTE images acquired with and without the off-resonance preparation pulse will accentuate the short  $T_2^*$  components.

Phase differences between tissues and tissue components can also be used to generate contrast with UTE imaging. Phase evolution has been shown to occur during the RF pulse and readout periods of the UTE sequence (22). Phase images may generate more contrast than magnitude images (18) and susceptibility-weighted images can also be performed when both are combined.

Fat suppression can be important to increase conspicuity of musculoskeletal tissues. Unfortunately, a chemically selective technique, which is the most commonly used in clinical practice, is problematic when the objective is to image short  $T_2^*$  tissues. The broad spectral linewidths of the short  $T_2^*$  components overlap with the main fat peak and the fat-saturation pulse may inadvertently cause direct saturation of the components of interest. The combination of UTE with a chemical shift-based water-fat separation method (iterative decomposition of water and fat with echo asymmetry and least-squares estimation, IDEAL) has been successfully implemented to overcome this challenge (23). The UTE-IDEAL sequence uses multiple echoes which not only allow for multifrequency fat spectral modeling, but also provides quantitative  $T_2^*$  information.

### Quantitative Imaging

$T_2^*$  relaxation time is dependent on interactions between spins, tissue hydration, and susceptibility effects (24).  $T_2^*$  quantification is made possible with the acquisition of a series of images with constant repetition time (TR) and variable TE. Tissues with short  $T_2^*$  can be quantified with the UTE sequence. However, increases in TE result in different patterns of eddy currents, leading to variations in slice profile and different degrees of long  $T_2^*$  contamination (25). A number of approaches have been used to reduce errors (18,26). Additionally, quantification of short  $T_2^*$  signal has been performed following long  $T_2^*$  suppression (16).

$T_2^*$  can be calculated with a monoexponential decay model or with a multiexponential decay model. While multiexponential  $T_2^*$  analysis may provide unique and useful information, a number of challenges exist.

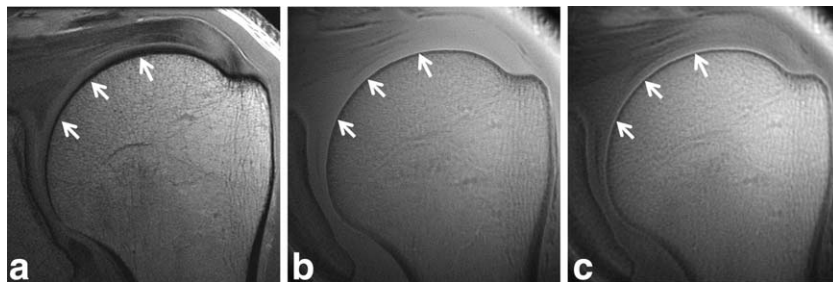


**Figure 3.** Coronal oblique images of the left shoulder. High-resolution conventional FSE sequence with 23 msec TE (a) shows no signal from the calcified cartilage (arrows). 2D-UTE image with  $8 \mu\text{s}$  TE (b) shows signal but poor contrast from the calcified cartilage (arrows).  $T_1$ -weighted saturation recovery image with 2D-UTE acquisition (c) highlights the calcified cartilage (arrows).

Table 1  
Approximate  $T_2^*$  Analysis and Composition of Select Musculoskeletal Tissues

	Biexponential $T_2^*$ analysis				Composition				Refs.	
	Monoeponential UTE $T_2^*$	Short fraction	Short $T_2^*$	Long fraction	Long $T_2^*$	Water fraction	Collagen fraction (dry weight)	Proteoglycan fraction (dry weight)		Other (dry weight)
Cartilage	10–28 msec	18%	0.5 msec	82%	35 msec	65–80%	60%	12%		(28,38–40,53)
TMJ disc	8–19 msec					80%	62%	3%		(77,80)
Knee meniscus	5–8 msec	49%	2 msec	51%	19 msec	70%	60–70%	2–8%		(67,98)
Tendon	1–2 msec	70–90%	< 1 msec	10–30%	8–20 msec	66–75%	65–87%	0.2–5%		(28,81–84,99,100)
Bone (cortical)	0.4–0.8 msec	65–95%	0.3 msec	5–35%	2 msec	20%	30–35% (collagen and protein)		65–70% calcium phosphate	(16,54,61)

These include sensitivity to spatial resolution, image signal-to-noise ratio, the number and spacing of echoes, the number of fitting components, and the differences between component  $T_2^*$  values (27). Knowledge of the total number of components and transverse relaxation time of each individual component in a particular tissue is based on data acquired with high-performance spectroscopic systems using Carr–Purcell–Meiboom–Gill (CPMG) sequences and nonnegative least squares (NNLS) approaches. Although this allows for no a priori assumptions about the total number and  $T_2$  relaxation of components, it cannot be used to characterize short  $T_2$  tissues on clinical MR systems due to minimal TE limitations. It is assumed that the number and relationship between components made with CPMG and UTE sequences at various field strengths is similar, but UTE sequences will incorporate local susceptibility effects resulting in a shortening of  $T_2^*$  relative to  $T_2$ . Multicomponent analysis in humans is typically performed with the assumption of two components. Use of UTE sequences allows detection of a "short"  $T_2^*$  component (containing short and ultrashort components) and a "long"  $T_2^*$  component (28). In vivo bicomponent analysis has been successfully employed with multiple tissues of the musculoskeletal system (25) (Table 1).

The magic angle effect causes variations in transverse relaxation values dependent on collagen fiber orientation relative to  $B_0$  (29). Transverse relaxation is shortest when fibers are oriented at  $0^\circ$  and longest when they are oriented at  $54.7^\circ$ . While this phenomenon can be used to improve contrast, it confounds the quantitative evaluation of highly oriented collagen-rich tissues in the clinical setting. The magnitude of the effect on transverse relaxation depends on sequence type and parameters, but intensity variations greater than a factor of 10 have been demonstrated (29). Furthermore, results from spectroscopic systems have shown that both the total number and individual component  $T_2$  relaxation times vary depending on orientation in the magnet (30). Despite this, studies performed on clinical MR systems with bicomponent UTE  $T_2^*$  analysis suggest that fractional analysis is much less sensitive to magic angle effects compared with single component analysis (31). For instance, Pauli et al (31) showed that one histologically normal patellar cartilage specimen demonstrated CPMG-measured  $T_2$  values varying from 30.7 to 79.3 msec, dependent on fiber orientation with the main magnetic field. For the same full-thickness regions of interest (ROIs), short  $T_2^*$  water fractions ranged from 18.8 to 20.7%, appearing much less sensitive to the magic angle effect.

$T_1$  relaxation time is dependent on tissue water content and the macromolecular environment of the tissue (24). Rapid  $T_1$  quantification of short  $T_2^*$  tissues is possible with the UTE technique combined with a saturation recovery technique for 2D imaging (16,18) or with a variable flip angle (VFA) method for 3D imaging (32). The VFA method relies on the acquisition of 3D UTE datasets with two through six optimized flip angles. Both the saturation recovery and VFA methods demonstrate good agreement with each

other (33). Specifically, Wright et al (33) measured  $T_1$  values in volunteer Achilles tendons and mean  $T_1$  for the regions of interest were  $725 \pm 42$  msec and  $698 \pm 54$  msec for the saturation recovery and VFA UTE techniques, respectively, without significant difference between the two measurements.

$T_{1\rho}$  quantification allows for the assessment of extremely slow molecular motions (34).  $T_{1\rho}$  has been used to investigate large macromolecules such as proteoglycans and their characteristic polysaccharide chains known as glycosaminoglycans (GAGs). In  $T_{1\rho}$  imaging, longitudinal magnetization is brought into the transverse plane with a  $90^\circ$  pulse and subsequently locked with a spin-lock pulse. During the locking pulse, magnetization relaxes by the time constant  $T_{1\rho}$ . A  $-90^\circ$  pulse is then delivered to flip the magnetization back into the longitudinal plane with subsequent delivery of a crusher gradient to spoil residual transverse magnetization. Magnetization stored in the longitudinal axis is then read out by the UTE sequence, which allows for measurements to be made in short  $T_2^*$  tissues.  $T_{1\rho}$  is quantified by repeating the experiment with various spin lock times and fitting the data to an exponential equation (3).

Magnetization transfer (MT) contrast is based on interactions between the free and restricted proton pools. MT may provide unique information about the microscopic and chemical environment. The MT sequence employs an off-resonance RF saturation pulse, which is typically far from the narrow peak of free water. The RF pulse affects the short  $T_2^*$  components, which have broad spectral linewidths. Exchange with the free water pool leads to a loss of longitudinal magnetization. Combination with the UTE sequence allows for the assessment of the MT effect in short  $T_2^*$  tissues. The MT ratio (MTR) is a useful measure to quantify the MT effects and is derived from one image without the MT preparation pulse ( $M_0$ ) and one image with the MT pulse ( $M_{SAT}$ ).

$$MTR = \frac{M_0 - M_{SAT}}{M_0} \quad [1]$$

Measurement of MT is particularly challenging with short  $T_2^*$  tissues since the RF pulse may directly saturate the free proton pool (35). Furthermore, MT measurements are sensitive to many technical variables and are highly dependent on the specific imaging parameters of the applied pulse sequence. When comparing longitudinal measurements of MTR, one should use the same frequency and power values for the off-resonance pulse. Additionally, the same field strength should be used since MTR is affected by  $T_1$  relaxation time and therefore measurements at 3T are expected to yield slightly lower values compared with 1.5T (36). MTR is much less sensitive to magic angle effects compared with transverse relaxation times (37).

## APPLICATIONS

To date, UTE sequences have been used to study many tissues of the musculoskeletal system. This sec-

tion will focus on anatomical considerations unique to individual tissues as well as review qualitative and quantitative clinical applications.

## Articular Cartilage

### Anatomical Considerations

Articular cartilage refers to hyaline cartilage which lines the ends of the bones in diarthrodial joints. Chondrocytes are scarce in cartilage, but are responsible for producing and maintaining the extracellular matrix (ECM). Cartilage is composed of  $\sim 65$ – $80\%$  water (38) and of the dry weight,  $\sim 60\%$  is collagen and  $12\%$  is sulfated proteoglycan (39,40). Collagen fibrils are predominantly composed of type II collagen. Type X collagen is found in calcified cartilage (41). Aggrecan is the major proteoglycan in articular cartilage, containing chondroitin sulfate and keratan sulfate (GAG) chains.

Articular cartilage can roughly be separated into four zones: the most superficial zone, tangential zone, middle zone, and deep zone (42,43). In general, collagen fibrils vary from being fine and parallel at the articular surface to thicker and perpendicular at the deep zone (44). Furthermore, the collagen network has a preferred orientation known as the split-line direction. Proteoglycan content also shows depth variation, increasing with depth from the surface (45).

The deep zone of cartilage is attached to subchondral bone through a metabolically active region of calcified cartilage, ranging from  $79$ – $243 \mu\text{m}$  in thickness (46). With advancing age, the calcified cartilage decreases in thickness. In addition, the number of tidemarks, which represents the junction between the calcified and uncalcified cartilage, also increases with advancing age such that after age 70 nearly all tidemarks will be duplicated, with up to four being present (46).

### Imaging

Cartilage has a high fraction of long  $T_2^*$  components and therefore cartilage demonstrates high signal with both conventional and UTE sequences. However, with the UTE sequence signal is also obtained from the short  $T_2^*$  components. Of particular interest is the calcified layer of cartilage, which may be involved in the pathogenesis of chondral degeneration (47). The UTE sequence has been shown to be sensitive to the presence of the calcified cartilage layer (48), largely due to short  $T_1$  relaxation. With subtraction or application of preparation pulses such as single or double inversion recovery, selective visualization of the calcified layer can be achieved (19) (Fig. 4).

Studies performed with articular cartilage on spectroscopic systems suggest that there are up to four pools of protons, each with distinct relaxation times, including bulk water, water trapped between collagen fibers, water associated with proteoglycans, and water associated with collagen (49). The UTE sequence allows for detection of all components except for water associated with collagen, which has supershort

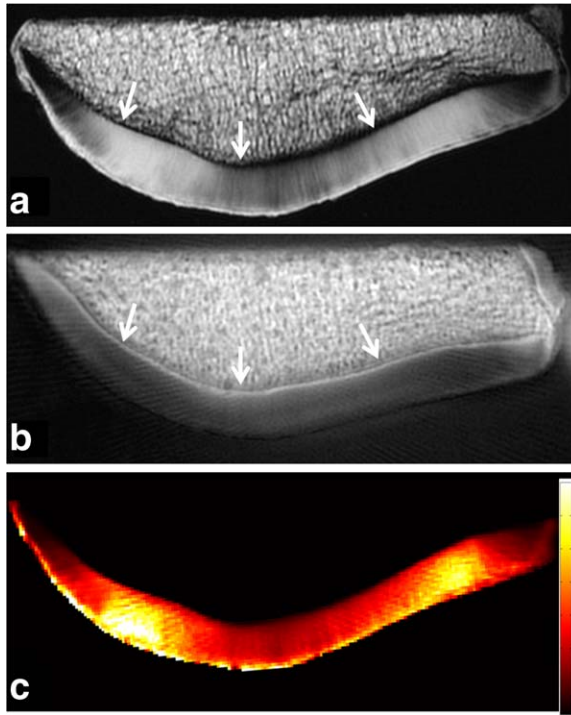


**Figure 4.** Axial MR images of a patella. High-resolution spin-echo sequence with 38 msec TE (a) shows no signal from the deep radial and calcified cartilage (arrows). 8  $\mu$ s minus 5 msec subtraction image (b) highlights the calcified layer of cartilage (arrows). Pixel map of monoexponential  $T_2^*$  values generated from UTE images (c) with biexponential analysis yielding short  $T_2^*$  of 0.7 msec, short fraction 23%, long  $T_2^*$  37.7 msec, and long fraction 77% (plot not shown).

transverse relaxation ( $T_2^*$  less than 20  $\mu$ s) (50). Compared with conventional sequences, detection of these additional components may be useful in determining early stages of disease. Using a monoexponential decay model, Williams et al (51) found that UTE- $T_2^*$  values were more sensitive to matrix degeneration compared with conventional  $T_2$  values based on histological standards. However, in contrast to conventional techniques, the UTE- $T_2^*$  values decreased with increasing degeneration.

It has been shown that four types of  $T_2^*$  decay patterns can be visualized on clinical MR systems (52), but a bicomponent model is the best that can be achieved within clinically allowable imaging times and may be sufficient to describe the decay pattern in cartilage (50). Pauli et al (31) found a significant correlation between increasing short  $T_2^*$  fractions and worsening degrees of degeneration.

Evaluation of reproducibility is an integral part of the validation of new imaging techniques. There are limited studies to date presenting reproducibility data for quantitative measures with the UTE techniques. However, one study performed by Williams et al (53) imaged 11 asymptomatic subjects on 3 consecutive days using UTE- $T_2^*$  mapping and found intersession precision error of 8% which corresponded to a mean  $T_2^*$  of 1.2 msec. Intraobserver reliability was also assessed in the same study and was found to be excellent.

## Bone

### Anatomical Considerations

Bone is composed of  $\sim$ 15% water by volume, either bound to collagen or residing within spaces, and 85% type I collagen and calcium hydroxyapatite (54). From a structural perspective, the periosteum, cortical bone, trabecular bone, and marrow elements are distinct.

Periosteum is a membrane that covers the outer surface of nearly all bones except at the joints. It is composed of a superficial fibrous layer and an inner, thinner osteogenic layer (55). Total periosteal thickness in human mid-diaphyseal regions is about 100  $\mu$ m for both tibia and femora, with mean fibrous layer thicknesses of 72–77  $\mu$ m and mean inner layer thickness of 29–23  $\mu$ m (56). Cortical bone is the dense outer layer, composing  $\sim$ 80% of the total mass of the adult skeleton, with  $\sim$ 5–10% porosity (57). Cortical bone pores consist of Haversian canals, Volkmann's canals, resorption cavities, lacuna, and canaliculi. These are occupied by blood vessels, nerves, or osteocytes. Trabecular bone is predominantly found in the axial skeleton as well as near the joints of long bones and demonstrates 75–95% porosity (57). It consists of a 3D structure of interconnected plates and rods, filled with bone marrow. Bone marrow may be red or yellow, each with a different chemical composition. Red marrow contains  $\sim$ 40% fat, 40% water, and 20% protein and yellow marrow contains  $\sim$ 80% fat, 15% water, and 5% protein (58). Precise composition of marrow varies by location and is dependent on age, gender, individual health, and other variables.

### Imaging

Normal periosteum as well as alterations due to age, acute fracture, or chronic injury can be readily visualized with UTE imaging (55). Although reported monoexponential  $T_2^*$  values for adult periosteum range from 5–11 msec, there is a sufficiently high proportion of short  $T_2^*$  components that signal is readily seen on subtraction between UTE and longer TE images (55).

Studies performed with cortical bone on spectroscopic systems have found three pools of protons, including collagen methylene protons, collagen-bound water, and a broad peak consisting of pore water and lipid (59). UTE sequences can detect all but collagen methylene protons, whose  $T_2^*$  values are supershort (less than 50  $\mu$ s) (60). Monoexponential  $T_2^*$  values obtained with the UTE sequence have been reported to range from 0.39–0.5 msec (16,61). Separation of collagen-bound water from pore water is important since the two are associated with different contributions to bone quality and strength. Expansion of pore volume due to aging or osteoporosis weakens bone (59).

A wide variety of UTE-based techniques have been used to qualitatively and quantitatively evaluate the components of cortical bone water (18). Based on relaxation differences, clinically compatible techniques that can distinguish between bound and pore water include use of bicomponent analysis, single adiabatic inversion, or double adiabatic inversion (62) (Fig. 5). More recently, two UTE-derived indices that



**Figure 5.** Axial MR images through the leg of a healthy volunteer. Clinical gradient echo sequence (a) shows a signal void in the region of the tibial cortex (arrow). The UTE sequence (b) shows slightly higher signal from the tibial cortex (arrow), but poor contrast due to the high signal from the surrounding muscle and fat which limit the dynamic range for cortical bone. The IR-UTE sequence (c) selectively suppresses signal from fat and muscle creating high contrast for the short  $T_2^*$  components of cortical bone (arrow). An eraser (dashed arrows) with known  $T_1$  and  $T_2^*$  values ( $\sim 200$  msec and  $300 \mu\text{s}$ , respectively) was placed for reference.

have been significantly correlated with micro-CT porosity are the *porosity index* (63) and *suppression ratio* (64), both which have the potential to be readily implemented into clinical practice. The porosity index is calculated from two acquisitions, one with an  $50 \mu\text{s}$  TE, capturing signal from pore water and collagen-bound water, and a second with a 1.2 msec TE, capturing only signal from pore water. Porosity index is defined as the ratio of mean intensity in the 1.2 msec TE image to that of the  $50 \mu\text{s}$  TE image. The suppression ratio is also calculated from two acquisitions, one image with long  $T_2^*$  suppression and an unsuppressed image. The suppression ratio is defined as the ratio of mean intensity between the unsuppressed to suppressed images. The concept is that suppression will increase with increasing pore sizes, which are associated with longer  $T_2^*$  values.

UTE techniques have not been as widely explored for trabecular bone and bone marrow as they have for cortical bone. Direct imaging of ex vivo trabecular bone architecture has been performed using a ZTE sequence (65). In the presence of trabeculae, bone marrow  $T_2^*$  relaxation time shortens due to magnetic field inhomogeneities. In this setting, UTE techniques may be useful to measure the effective  $T_2^*$  as a surrogate for trabecular density. UTE-IDEAL could potentially be used for the evaluation of bone marrow composition.

Surrogate measures for bone porosity have shown promising reproducibility data. Rad et al (66) measured bone water concentration in 10 subjects twice within 2 months and found an intraclass correlation coefficient of 0.95. Studies using the suppression ratio have also found high reproducibility with an intraclass correlation coefficient of 0.99 (64).

## Menisci of the Knee

### Anatomical Considerations

The menisci of the knee are semilunar-shaped fibrocartilaginous structures. They are composed of  $\sim 70\%$  water and of the dry weight,  $\sim 60\text{--}70\%$  is collagen and 2–8% is proteoglycan (67). There are at least six well-defined fiber groups within the meniscus, including the surface meshwork, lamella, circumferential, radial, vertical, and meshwork fibers around the circumferential fibers (68,69). The circumferential bundles are the largest fiber group, mainly composed of collagen type I, and are continuous into the

root ligaments. The radial fibers are another prominent fiber group, which may appear as larger collagen bundles (radial ties) or sheets (70). Radial fibers mainly consist of type I collagen and extend from the peripheral margin of the meniscus towards the free edge, and are generally horizontal in direction. Proteoglycan content also vary by region, with a higher content at the central portion compared with the peripheral portion (71). The adult meniscus is vascularized at the peripheral 10–25%, but avascular at the more central portions (72).

### Imaging

UTE can be used to demonstrate individual fiber groups. Additionally, meniscal calcifications can be imaged and quantified (73). Increased monoexponential  $T_2^*$  values may indicate subclinical meniscus degeneration (74). UTE with bicomponent analysis has also been successfully applied to the meniscus (28) and can be useful in quantifying normal versus abnormal meniscal regions (Fig. 6).  $T_{1\rho}$  relaxation may be sensitive to changes in proteoglycan and GAG content and UTE- $T_{1\rho}$  has been applied to the meniscus (3). The vascularized portions of the meniscus and meniscal root ligaments can be visualized in vivo with UTE imaging after intravenous contrast administration (Fig. 7).

## Temporomandibular Joint

### Anatomical Considerations

The temporomandibular joint (TMJ) is one of the most complex and essential joints in the body. The osseous components include the mandibular condyle and the mandibular fossa, which is a concave depression in the squamous portion of the temporal bone. The articular disc typically separates the two bones from direct contact. The articular surfaces of the bones are covered with fibrocartilage which, when compared with hyaline articular cartilage, is less susceptible to the effects of aging and allow for improved healing capacity (75). The TMJ is capable of active remodeling throughout life, including the articular fibrocartilage which maintains the balance between physiologic and pathologic responses (76).

The fibrocartilaginous surfaces of the mandibular condyle and fossa contain water, collagen, and proteoglycan. Although the exact percentages have not been well studied, collagen is the most abundant extracellular matrix constituent. TMJ discs are composed of

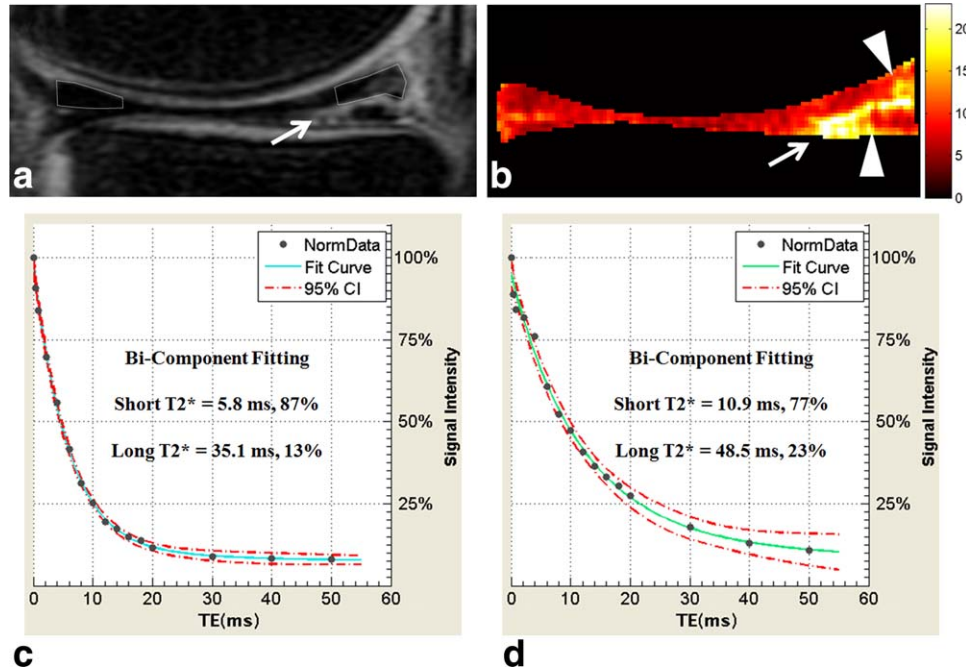


**Figure 6.** A 40-year-old patient with longitudinal-horizontal tear of the posterior horn of the medial meniscus. Conventional sagittal-oblique MR image with 38 msec TE (a) shows meniscus tear (arrow). Monoexponential  $T_2^*$  map generated from UTE images (b) highlights regions of degeneration (arrowheads) adjacent to the tear (arrow). Quantitative biexponential fitting through the superior halves of the normal anterior horn (c) and degenerated posterior horn (d) shows notable differences in the degenerated portion with longer short  $T_2^*$  time and smaller short  $T_2^*$  fraction confirming degenerative tear.

~80% water and the dry weight is composed of ~62% collagen and 3% GAG (77).

#### Imaging

3D UTE images have been used to evaluate condylar shape and can readily visualize the fibrocartilaginous surface (78). The TMJ disc contains a sufficiently large long  $T_2^*$  component that it can be readily detected with conventional spin-echo imaging. However, with UTE imaging,  $T_2^*$  contrast can be optimized between the disc and lamina (79). Quantitative  $T_2^*$  values have been generated for the TMJ discs and condylar fibro-

cartilage (80) (Fig. 8). Increasing UTE  $T_2^*$  values of TMJ disc have correlated with lower indentation stiffness (softer disc) and less collagen orientation, as indicated by polarized light microscopy (80). Quantitative UTE  $T_2^*$  maps can facilitate characterization of the individual portions of the TMJ disc (Fig. 9).

#### Tendons, Ligaments, and Entheses

##### Anatomical Considerations

Tendon composition varies by anatomic location in addition to health. Total water content of healthy

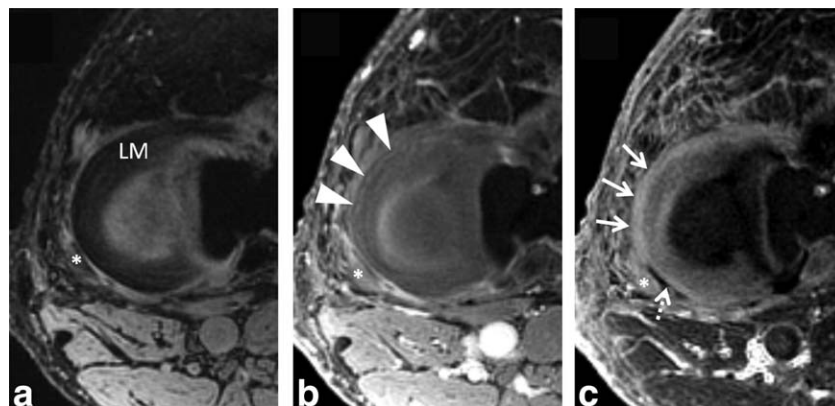


**Figure 7.** Axial MR images through the lateral meniscus of a healthy volunteer. Clinical gradient echo sequence with 12 msec TE (a) shows the C-shaped lateral meniscus (LM). 3D UTE-Cones image with 30  $\mu$ s TE (b) was obtained 1 minute after intravenous gadolinium contrast administration, showing early perfusion to the peripheral meniscus (arrowheads). A 30- $\mu$ s minus 12-msec subtraction image generated from dual-echo 3D UTE-Cones source images (c) 46 minutes after contrast administration shows diffusion of gadolinium into the peripheral meniscus (thin arrows). Note relatively avascular region at the popliteal hiatus (dashed arrow). Popliteus tendon is marked with an asterisk.

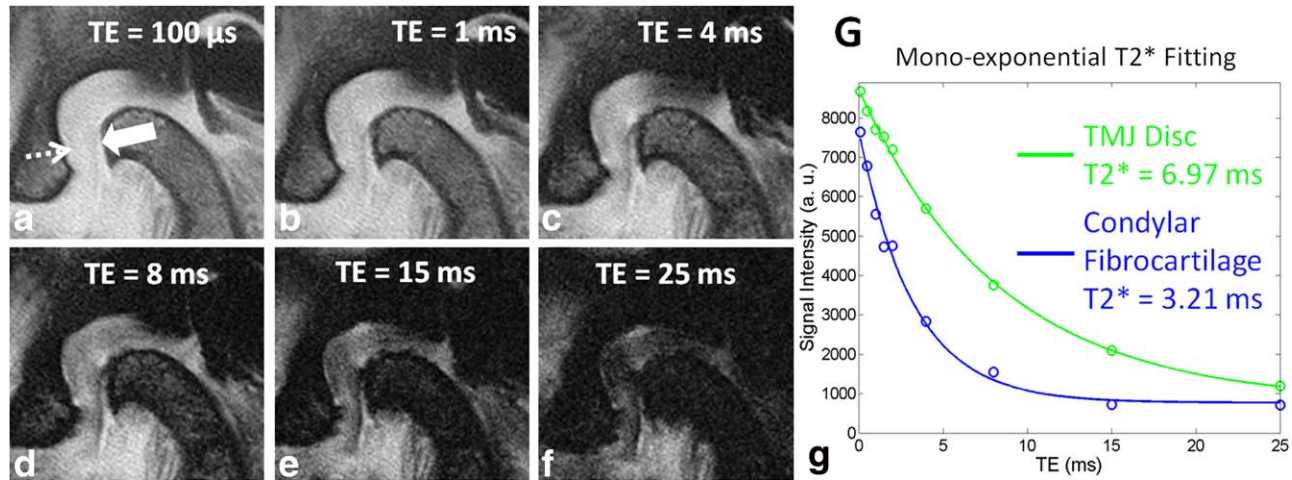


**Figure 8.** Sagittal MR images through the TMJ. Select multiecho images ranging from 100  $\mu$ s to 25 msec (a–f) show condylar fibrocartilage (solid arrow) and TMJ disc (dashed arrow). Monoexponential  $T_2^*$  fitting curve (g) shows excellent curve fitting with  $T_2^*$  values of 6.97 msec and 3.21 msec for the disc and fibrocartilage, respectively.

Achilles tendons is  $\sim 66\%$  (81), whereas normal rotator cuff tendons contain about 75% water (82). Of the dry weight of tendon,  $\sim 65$ –87% is collagen (mainly type I) and 0.2–5% is GAG (83,84). In regions subject primarily to tension, such as the tensile zone of the Achilles, collagen content is higher and GAG content is lower. In regions also subject to pressure, such as the rotator cuff or near the entheses (where soft tissue connects to bone), collagen content is lower and GAG content is higher. Ligaments are grossly similar to tendons, but contain slightly lower amounts of collagen and more GAGs (84).

Tendon and ligaments are highly ordered due to the assembly of type I collagen into fibrils that aggregate to form larger fiber bundle units. Endotenon and endoligament invest and bind the collagen fibers together, and also serve as a conduit for neurovascular structures (83,85). Regions of fibrocartilage or fat can be found within tendons, ligaments, and entheses

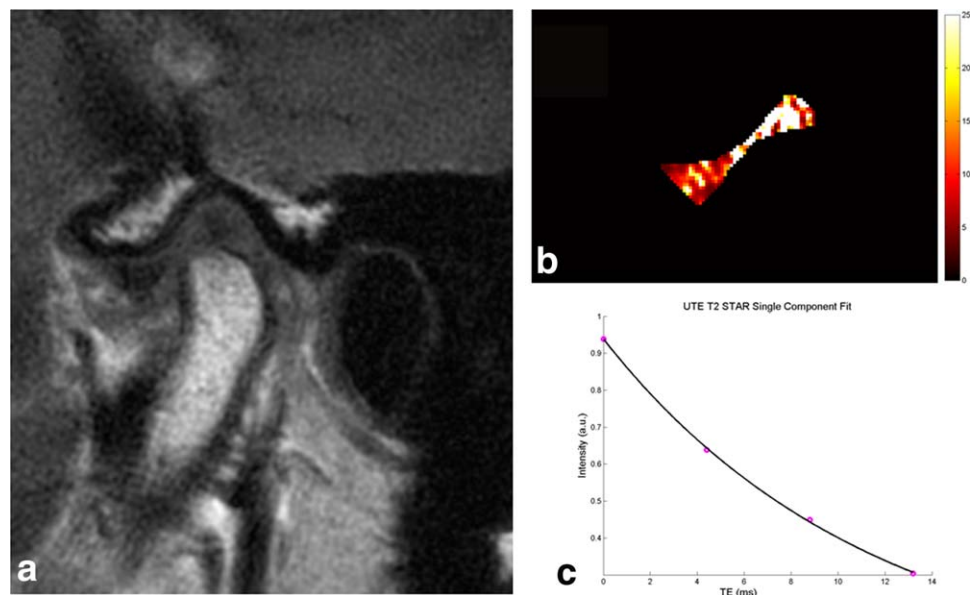
at sites subject to compression, such as within the distal Achilles, rotator cuff, or tibialis posterior (86).

Tendon degeneration is a necessary precursor to tendon tearing. Degenerated tendons demonstrate higher total water content, decrease in collagen content, collagen fiber disruption, and GAG accumulation (81,82,87). Fibrocartilaginous metaplasia and an accumulation of other substances such as mucous, fat, and eosinophils can also be seen in degeneration (87). Entheses are a characteristic site of involvement with spondyloarthropathies (88).

### Imaging

Tendons, ligaments, entheses, and their individual components can be readily visualized with the UTE sequence (89). Differences in relaxation between collagen fascicles (shorter  $T_2^*$ ) and endotenon, endoligament, and fibrocartilage (longer  $T_2^*$ ) can be used to

**Figure 9.** Temporomandibular joint disc of a 35-year old asymptomatic volunteer. Conventional  $T_1$ -weighted fast-spin echo image with mouth closed (a) shows the normal position of the TMJ disc. Quantitative pixel map generated from UTE images (b) show increased  $T_2^*$  values at the intermediate zone and posterior band, suggestive of early-stage degeneration. Monoexponential  $T_2^*$  analysis of the entire disc (c) shows excellent curve fitting with  $T_2^*$  value of 11.4 msec.



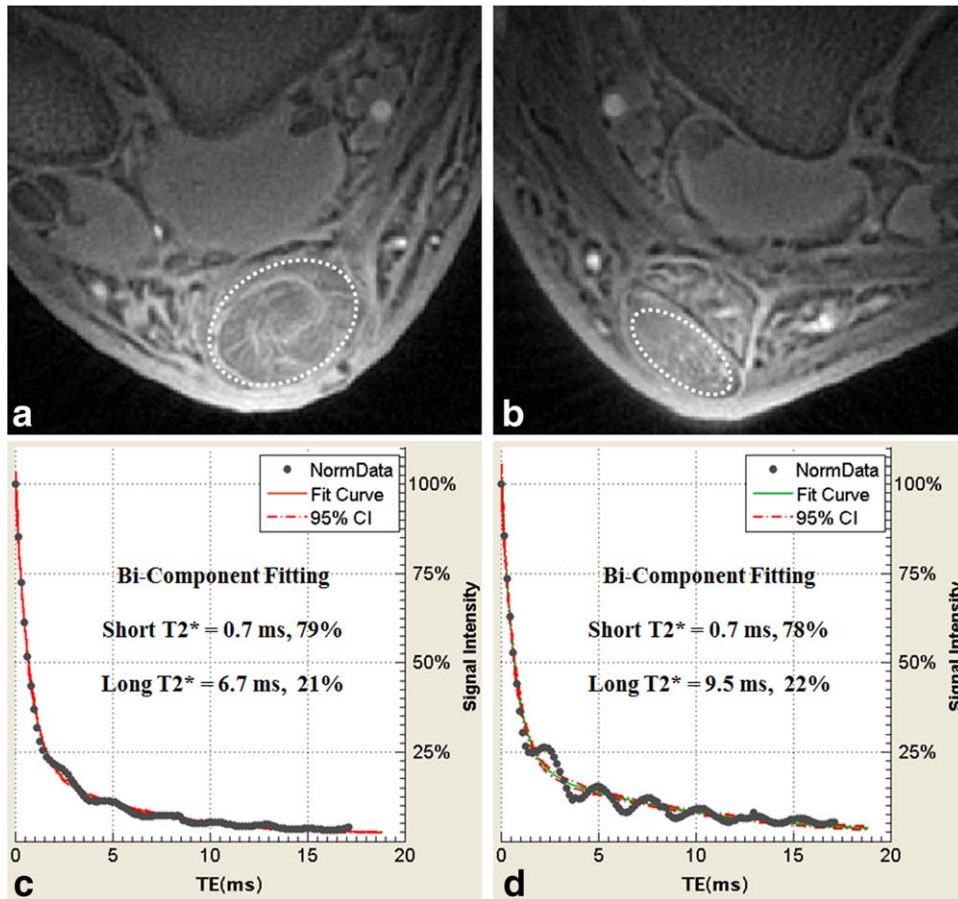


**Figure 10.** A 60-year-old man several years after successful right Achilles tendon repair. Axial UTE MR images of the repaired right Achilles tendon (a) compared with the same patient's asymptomatic left Achilles tendon (b). Quantitative bi-component analysis performed in the tendons (dashed ovals) show that the short  $T_2^*$  value and fraction of the repaired right tendon (c) has approached the asymptomatic left side (d), confirming adequate collagen remodeling.

create internal contrast. Tendon alterations which are subtle or not visible at higher TEs are readily visible on UTE images with or without exogenous contrast enhancement (89).

Studies performed with tendon on spectroscopic systems suggest that there are up to four pools of protons (90), although many other studies have found three, likely corresponding to tightly bound water, weakly bound water, and free water (30). The number of components and  $T_2^*$  values vary depending tendon orientation and spatial resolution (30). Biexponential  $T_2^*$  analysis has been successfully performed in vivo using both UTE and  $\nu$ TE sequences, and fractions and  $T_2^*$  values vary depending on tendon location, consistent with different tendon compositions. More recently, Juras et al (91) found biexponential  $T_2^*$  values to be more useful for distinguishing between healthy volunteers and patients with Achilles tendinopathy compared with monoexponential values. Bicomponent analysis can also be useful in quantifying the injured or postoperative tendon (Fig. 10).

### Intervertebral Disc

#### Anatomical Considerations

The intervertebral discs of the spine contain a central nucleus pulposus surrounded by a peripheral annulus fibrosus. Healthy nucleus pulposi contain about 70–90% water and of the dry weight, 65% is proteo-

glycan and 15–20% is type II collagen (92). The annulus fibrosus contains about 60–70% water and of the dry weight, 20% is proteoglycan and 50–60% is collagen (92). The collagen of the annulus is also highly ordered, forming more than 20 concentric lamellar sheets. The individual lamellae within a disc alternate in orientation, approximately  $\pm 25^\circ$  relative to the endplates (93).

The cartilaginous endplate (CEP) is an  $\sim 0.6$ –1 mm thick layer of hyaline-like cartilage that forms an interface between the intervertebral disc and the vertebral body. The CEP is strongly attached to the annulus fibrosus, but only weakly attached to the vertebral body, which is why it is predominantly considered a component of the disc (94). Similar to hyaline cartilage at other sites, the deep zone of the CEP attaches to bone through a thin layer of calcified cartilage. The intervertebral disc is avascular and blood vessels in the bone and longitudinal ligaments serve as routes for nutrients and waste. Solutes move by diffusion through the CEP and annulus fibrosus. Calcification of the CEP with advancing age or degeneration may hinder nutrition of the intervertebral disc and result in deterioration of biomechanical integrity (95).

#### Imaging

Studies performed with spectroscopic systems suggest that there are four water components in both the

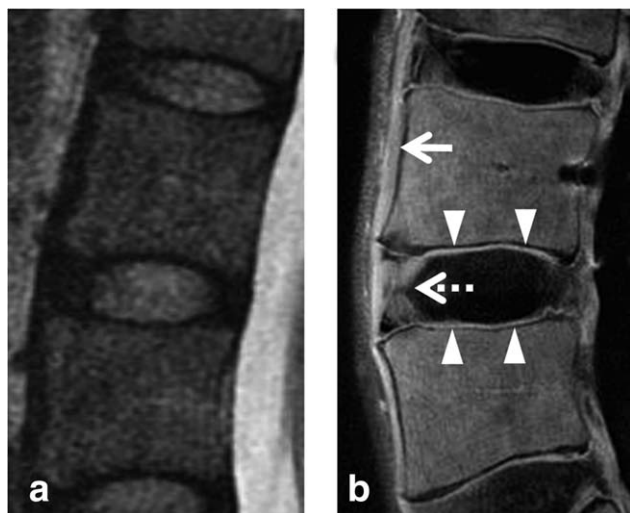


**Figure 11.** Lumbar spine imaged with conventional  $T_2$ -weighted FSE sequence (a) and UTE subtraction image (b) generated from  $10 \mu\text{s}$  TE minus 10 msec TE. Short  $T_2^*$  components are directly visible in the anterior longitudinal ligament (arrow), outer annulus fibrosus (dashed arrow), and cartilaginous endplate (arrowheads) on UTE subtraction image, but not on the conventional image. Images courtesy of Won C. Bae, PhD.

nucleus pulposus and annulus fibrosus (96), likely corresponding to water tightly bound to collagen, water loosely bound to collagen, water associated with residue proteins, and water associated with GAG. Healthy nucleus pulposi were shown to contain a majority of water associated with GAG, whereas healthy annuli were shown to contain a majority of water loosely bound to collagen and associated with residue proteins (96).

UTE techniques allow for visualization of components of the intervertebral disc that cannot be directly seen with conventional techniques. These include the longitudinal ligaments, annulus fibrosus, and the CEP (Fig. 11). The uncalcified and calcified portions of the CEP can be visible with UTE images, creating a bilaminar appearance (97).

## CHALLENGES

We have summarized various qualitative and quantitative UTE techniques as well as potential applications in the musculoskeletal system. Notably, there are relatively few clinical studies to date using UTE techniques. This highlights a number of challenges that are continuously being improved upon. Challenges to clinical translation can be broken up into three categories, including hardware limitations, software availability, and validation studies.

Hardware continues to improve and many challenges are relatively solvable, such as sufficiently fast transmit-receive switches and precise RF waveform transmission. One of the most important challenges to UTE imaging is the requirement for high gradient performance. Unfortunately, this problem is more difficult to solve. In particular, gradient waveforms are often far from ideal due to current induc-

tion from the rapidly switching gradients (eddy currents). Short-term eddy currents disturb the UTE measurement in a number of complicated ways (26). These can be improved with gradient calibration, minimized with certain imaging tactics, or overcome with more complex pulse sequences. For instance, positioning at the magnet isocenter typically results in improved image quality. This is clearly easier to obtain with peripheral joints such as the ankle compared with more centrally located joints such as the shoulder or hip. Imaging more spherical or cylindrical parts such as the leg will decrease susceptibility and typically result in higher image quality compared with less cylindrical body parts such as the fingers with the many air-tissue interfaces. Removal of the slice-select gradient with the use of 3D imaging together with a short rectangular excitation pulse also decreases eddy currents.

Software availability is another major challenge to widespread use. At the time of this article, there are no product UTE-type sequences available, although nearly all major vendors have a near-product UTE sequence in development. Furthermore, the near-product sequences are typically qualitative and used for morphologic or anatomic analysis. Cross-platform quantitative sequences are scarcer. Finally, there are relatively few validation and reproducibility studies compared with feasibility studies, in part because they are more time-consuming and expensive. However, as shown in this article, these types of studies are occurring and the results are quite encouraging.

In summary, the UTE sequence and its modifications should be considered as complementary to conventional MR techniques and may allow for improved evaluation of the musculoskeletal system. Tissues with short mean  $T_2^*$  and short  $T_2^*$  components can now be qualitatively highlighted or quantitatively evaluated. Clinical translation of UTE techniques is likely to occur in the near future and ongoing research will provide validation for widespread use.

## REFERENCES

- Bydder GM. Review. The Agfa Mayneord lecture: MRI of short and ultrashort  $T(2)$  and  $T(2)^*$  components of tissues, fluids and materials using clinical systems. *Br J Radiol* 2011;84:1067-1082.
- Pauly JM, Conolly SI, Nishimura D, Macovski A. Slice-selective excitation for very short  $T_2$  species. In: *Proc 8th Annual Meeting ISMRM, Amsterdam; 1989* (abstract 28).
- Du J, Carl M, Diaz E, et al. Ultrashort TE  $T_1\rho$  (UTE  $T_1\rho$ ) imaging of the Achilles tendon and meniscus. *Magn Reson Med* 2010;64:834-842.
- Rahmer J, Bornert P, Groen J, Bos C. Three-dimensional radial ultrashort echo-time imaging with  $T_2$  adapted sampling. *Magn Reson Med* 2006;55:1075-1082.
- Pauly JM. Selective excitation for ultrashort echo time imaging. *eMagRes: John Wiley & Sons; 2012*.
- Du J, Bydder M, Takahashi AM, Chung CB. Two-dimensional ultrashort echo time imaging using a spiral trajectory. *Magn Reson Imaging* 2008;26:304-312.
- Gurney PT, Hargreaves BA, Nishimura DG. Design and analysis of a practical 3D cones trajectory. *Magn Reson Med* 2006;55:575-582.
- Qian Y, Boada FE. Acquisition-weighted stack of spirals for fast high-resolution three-dimensional ultra-short echo time MR imaging. *Magn Reson Med* 2008;60:135-145.

9. Song HK, Wehrli FW. Variable TE gradient and spin echo sequences for in vivo MR microscopy of short T2 species. *Magn Reson Med* 1998;39:251–258.
10. Weiger M, Pruessmann KP. MRI with zero echo time. *eMagRes: John Wiley & Sons*; 2012.
11. Garwood M, Idiyatullin D, Corum CA, et al. Capturing signals from fast-relaxing spins with frequency-swept MRI: SWIFT. *eMagRes: John Wiley & Sons*; 2012.
12. Grodzki DM, Jakob PM, Heismann B. Ultrashort echo time imaging using pointwise encoding time reduction with radial acquisition (PETRA). *Magn Reson Med* 2012;67:510–518.
13. Weiger M, Brunner DO, Wyss M, Dietrich BE, Wilm BJ, Pruessmann KP. ZTE Imaging with T1 contrast. In: *Proc 22nd Annual Meeting ISMRM, Milan*; 2014 (abstract 4262).
14. Ida M, Wakayama T, Nielsen ML, Abe T, Grodzki DM. Quiet T1-weighted imaging using PETRA: initial clinical evaluation in intracranial tumor patients. *J Magn Reson Imaging* 2014 [Epub ahead of print].
15. Du J, Bydder M, Takahashi AM, Carl M, Chung CB, Bydder GM. Short T2 contrast with three-dimensional ultrashort echo time imaging. *Magn Reson Imaging* 2011;29:470–482.
16. Du J, Carl M, Bydder M, Takahashi A, Chung CB, Bydder GM. Qualitative and quantitative ultrashort echo time (UTE) imaging of cortical bone. *J Magn Reson* 2010;207:304–311.
17. Wu Y, Ackerman JL, Chesler DA, Graham L, Wang Y, Glimcher MJ. Density of organic matrix of native mineralized bone measured by water- and fat-suppressed proton projection MRI. *Magn Reson Med* 2003;50:59–68.
18. Du J, Bydder GM. Qualitative and quantitative ultrashort-TE MRI of cortical bone. *NMR Biomed* 2013;26:489–506.
19. Du J, Carl M, Bae WC, et al. Dual inversion recovery ultrashort echo time (DIR-UTE) imaging and quantification of the zone of calcified cartilage (ZCC). *Osteoarthritis Cartilage* 2013;21:77–85.
20. Du J, Takahashi AM, Bae WC, Chung CB, Bydder GM. Dual inversion recovery, ultrashort echo time (DIR UTE) imaging: creating high contrast for short-T(2) species. *Magn Reson Med* 2010;63:447–455.
21. Du J, Takahashi AM, Bydder M, Chung CB, Bydder GM. Ultrashort TE imaging with off-resonance saturation contrast (UTE-OSC). *Magn Reson Med* 2009;62:527–531.
22. Carl M, Chiang J-TA. Investigations of the origin of phase differences seen with ultrashort TE imaging of short T2 meniscal tissue. *Magn Reson Med* 2012;67:991–1003.
23. Wang K, Yu H, Brittain JH, Reeder SB, Du J. k-space water-fat decomposition with T2\* estimation and multifrequency fat spectrum modeling for ultrashort echo time imaging. *J Magn Reson Imaging* 2010;31:1027–1034.
24. Gore JC, Anderson AW. The physics of relaxation. *eMagRes: John Wiley & Sons*; 2013.
25. Du J. Quantitative ultrashort TE (UTE) imaging of short T2 tissues. *eMagRes: John Wiley & Sons*; 2012.
26. Lu A, Daniel BL, Pauly JM, Pauly KB. Improved slice selection for R2\* mapping during cryoablation with eddy current compensation. *J Magn Reson Imaging* 2008;28:190–198.
27. Xia Y. MRI of articular cartilage at microscopic resolution. *Bone Joint Res* 2013;2:9–17.
28. Du J, Diaz E, Carl M, Bae W, Chung CB, Bydder GM. Ultrashort echo time imaging with bicomponent analysis. *Magn Reson Med* 2012;67:645–649.
29. Fullerton GD, Cameron IL, Ord VA. Orientation of tendons in the magnetic field and its effect on T2 relaxation times. *Radiology* 1985;155:433–435.
30. Wang N, Xia Y. Anisotropic analysis of multi-component T2 and T1rho relaxations in Achilles tendon by NMR spectroscopy and microscopic MRI. *J Magn Reson Imaging* 2013;38:625–633.
31. Pauli C, Bae WC, Lee M, et al. Ultrashort-echo time MR imaging of the patella with bicomponent analysis: correlation with histopathologic and polarized light microscopic findings. *Radiology* 2012;264:484–493.
32. Springer F, Steidle G, Martirosian P, Syha R, Claussen CD, Schick F. Rapid assessment of longitudinal relaxation time in materials and tissues with extremely fast signal decay using UTE sequences and the variable flip angle method. *Invest Radiol* 2011;46:610–617.
33. Wright P, Jellus V, McGonagle D, Robson M, Ridgeway J, Hodgson R. Comparison of two ultrashort echo time sequences for the quantification of T1 within phantom and human Achilles tendon at 3 T. *Magn Reson Med* 2012;68:1279–1284.
34. Sepponen RE, Pohjonen JA, Sipponen JT, Tanttu JI. A method for T1 rho imaging. *J Comput Assist Tomogr* 1985;9:1007–1011.
35. Springer F, Martirosian P, Schick F. Magnetization transfer-ultrashort echo time (MT-UTE) imaging. *eMagRes: John Wiley & Sons*; 2012.
36. Stanisz GJ, Odobina EE, Pun J, et al. T1, T2 relaxation and magnetization transfer in tissue at 3T. *Magn Reson Med* 2005;54:507–512.
37. Hopfgarten C, Kirsch S, Reisig G, Kreinest M, Schad LR. Identification of in vitro degenerated porcine meniscal tissue: MTR contrast prevents misinterpretation due to the magic angle effect. In: *Proc 20th Annual Meeting ISMRM, Melbourne*; 2012 (abstract 1397).
38. Maroudas A. Physico-chemical properties of articular cartilage. In: Freeman MAR, editor. *Adult articular cartilage*, 2nd ed. Tunbridge Wells, UK: Pitman Medical; 1979. p 215–290.
39. Sophia Fox AJ, Bedi A, Rodeo SA. The basic science of articular cartilage: structure, composition, and function. *Sports Health* 2009;1:461–468.
40. Johnson D, Pedowitz RA. *Practical orthopaedic sports medicine and arthroscopy*. Philadelphia: Lippincott Williams & Wilkins; 2007.
41. Schmid TM, Linsenmayer TF. Immunohistochemical localization of short chain cartilage collagen (type X) in avian tissues. *J Cell Biol* 1985;100:598–605.
42. Hunziker EB, Michel M, Studer D. Ultrastructure of adult human articular cartilage matrix after cryotechnical processing. *Microsc Res Tech* 1997;37:271–284.
43. Fujioka R, Aoyama T, Takakuwa T. The layered structure of the articular surface. *Osteoarthritis Cartilage* 2013;21:1092–1098.
44. Aspden RM, Hukins DW. Collagen organization in articular cartilage, determined by X-ray diffraction, and its relationship to tissue function. *Proc R Soc Lond B Biol Sci* 1981;212:299–304.
45. Muir H. Proteoglycans of cartilage. *J Clin Pathol Suppl (R Coll Pathol)* 1978;12:67–81.
46. Lane LB, Bullough PG. Age-related changes in the thickness of the calcified zone and the number of tidemarks in adult human articular cartilage. *J Bone Joint Surg* 1980;62:372–375.
47. Boyde A, Riggs CM, Bushby AJ, McDermott B, Pinchbeck GL, Clegg PD. Cartilage damage involving extrusion of mineralisable matrix from the articular calcified cartilage and subchondral bone. *Eur Cell Mater* 2011;21:470–478.
48. Bae WC, Dwek JR, Znamirovski R, et al. Ultrashort echo time MR imaging of osteochondral junction of the knee at 3 T: identification of anatomic structures contributing to signal intensity. *Radiology* 2010;254:837–845.
49. Lattanzio PJ, Marshall KW, Damyanovich AZ, Peemoeller H. Macromolecule and water magnetization exchange modeling in articular cartilage. *Magn Reson Med* 2000;44:840–851.
50. Qian Y, Williams AA, Chu CR, Boada FE. Multi-component T2\* relaxation of knee cartilage under UTE acquisitions. In: *Proc 18th Annual Meeting ISMRM, Stockholm*; 2010 (abstract 830).
51. Williams A, Qian Y, Bear D, Chu CR. Assessing degeneration of human articular cartilage with ultra-short echo time (UTE) T2\* mapping. *Osteoarthritis Cartilage* 2010;18:539–546.
52. Qian Y, Williams AA, Chu CR, Boada FE. Multicomponent T2\* mapping of knee cartilage: technical feasibility ex vivo. *Magn Reson Med* 2010;64:1426–1431.
53. Williams A, Qian Y, Chu CR. UTE-T2\* mapping of human articular cartilage in vivo: a repeatability assessment. *Osteoarthritis Cartilage* 2011;19:84–88.
54. Wehrli FW, Song HK, Saha PK, Wright AC. Quantitative MRI for the assessment of bone structure and function. *NMR Biomed* 2006;19:731–764.
55. Reichert IL, Benjamin M, Gatehouse PD, et al. Magnetic resonance imaging of periosteum with ultrashort TE pulse sequences. *J Magn Reson Imaging* 2004;19:99–107.
56. Moore SR, Milz S, Knothe Tate ML. Periosteal thickness and cellularity in mid-diaphyseal cross-sections from human femora and tibiae of aged donors. *J Anat* 2014;224:142–149.

57. Martin RB, Burr DB, Sharkey NA. Skeletal tissue mechanics. New York: Springer; 1998.
58. Vande Berg BC, Malghem J, Lecouvet FE, Maldague B. Magnetic resonance imaging of normal bone marrow. *Eur Radiol* 1998;8:1327–1334.
59. Horch RA, Gochberg DF, Nyman JS, Does MD. Non-invasive predictors of human cortical bone mechanical properties: T(2)-discriminated H NMR compared with high resolution X-ray. *PLoS One* 2011;6:e16359.
60. Fernandez-Seara MA, Wehrli SL, Takahashi M, Wehrli FW. Water content measured by proton-deuteron exchange NMR predicts bone mineral density and mechanical properties. *J Bone Miner Res* 2004;19:289–296.
61. Techawiboonwong A, Song HK, Leonard MB, Wehrli FW. Cortical bone water: in vivo quantification with ultrashort echo-time MR imaging. *Radiology* 2008;248:824–833.
62. Horch RA, Gochberg DF, Nyman JS, Does MD. Clinically compatible MRI strategies for discriminating bound and pore water in cortical bone. *Magn Reson Med* 2012;68:1774–1784.
63. Bashoor-Zadeh M, Li C, Sun W, et al. Simple ultrashort echo time MRI measure associated with cortical bone porosity. In: Proc 21st Annual Meeting ISMRM, Salt Lake City; 2013 (abstract 1599).
64. Li C, Seifert AC, Rad HS, et al. Cortical bone water concentration: dependence of MR imaging measures on age and pore volume fraction. *Radiology* 2014 [Epub ahead of print].
65. Weiger M, Stampanoni M, Pruessmann KP. Direct depiction of bone microstructure using MRI with zero echo time. *Bone* 2013;54:44–47.
66. Rad HS, Lam SC, Magland JF, et al. Quantifying cortical bone water in vivo by three-dimensional ultra-short echo-time MRI. *NMR Biomed* 2011;24:855–864.
67. Blain E, Duance V. Meniscus. In: Hutson MA, Speed C, editors. Sports injuries. Oxford, New York: Oxford University Press; 2011. p 45–53.
68. Petersen W, Tillmann B. Collagenous fibril texture of the human knee joint menisci. *Anat Embryol* 1998;197:317–324.
69. Kambic HE, McDevitt CA. Spatial organization of types I and II collagen in the canine meniscus. *J Orthop Res* 2005;23:142–149.
70. Skaggs DL, Warden WH, Mow VC. Radial tie fibers influence the tensile properties of the bovine medial meniscus. *J Orthop Res* 1994;12:176–185.
71. Nakano T, Dodd CM, Scott PG. Glycosaminoglycans and proteoglycans from different zones of the porcine knee meniscus. *J Orthop Res* 1997;15:213–220.
72. Arnoczky SP, Warren RF. Microvasculature of the human meniscus. *Am J Sports Med* 1982;10:90–95.
73. Omoumi P, Bae WC, Du J, et al. Meniscal calcifications: morphologic and quantitative evaluation by using 2D inversion-recovery ultrashort echo time and 3D ultrashort echo time 3.0-T MR imaging techniques—feasibility study. *Radiology* 2012;264:260–268.
74. Williams A, Qian Y, Golla S, Chu CR. UTE-T2 \* mapping detects sub-clinical meniscus injury after anterior cruciate ligament tear. *Osteoarthritis Cartilage* 2012;20:486–494.
75. Wadhwa S, Kapila S. TMJ disorders: future innovations in diagnostics and therapeutics. *J Dent Educ* 2008;72:930–947.
76. Kuang B, Dai J, Wang Q-Y, et al. Combined degenerative and regenerative remodeling responses of the mandibular condyle to experimentally induced disordered occlusion. *Am J Orthodont Dentofac Orthoped* 2013;143:69–76.
77. Kuo J, Zhang L, Bacro T, Yao H. The region-dependent biphasic viscoelastic properties of human temporomandibular joint discs under confined compression. *J Biomechan* 2010;43:1316–1321.
78. Geiger D, Bae WC, Stature S, Du J, Chung CB. Quantitative 3D ultrashort time-to-echo (UTE) MRI and micro-CT (muCT) evaluation of the temporomandibular joint (TMJ) condylar morphology. *Skeletal Radiol* 2014;43:19–25.
79. Carl M, Sanal HT, Diaz E, et al. Optimizing MR signal contrast of the temporomandibular joint disk. *J Magn Reson Imaging* 2011;34:1458–1464.
80. Sanal HT, Bae WC, Pauli C, et al. Magnetic resonance imaging of the temporomandibular joint disc: feasibility of novel quantitative magnetic resonance evaluation using histologic and biomechanical reference standards. *J Orofac Pain* 2011;25:345–353.
81. de Mos M, van El B, DeGroot J, et al. Achilles tendinosis: changes in biochemical composition and collagen turnover rate. *Am J Sports Med* 2007;35:1549–1556.
82. Riley GP, Harrall RL, Constant CR, Chard MD, Cawston TE, Hazleman BL. Tendon degeneration and chronic shoulder pain: changes in the collagen composition of the human rotator cuff tendons in rotator cuff tendinitis. *Ann Rheum Dis* 1994;53:359–366.
83. Kannus P. Structure of the tendon connective tissue. *Scand J Med Sci Sports* 2000;10:312–320.
84. Amiel D, Frank C, Harwood F, Fronck J, Akeson W. Tendons and ligaments: a morphological and biochemical comparison. *J Orthop Res* 1984;1:257–265.
85. Villegas DF, Donahue TL. Collagen morphology in human meniscal attachments: a SEM study. *Connect Tissue Res* 2010;51:327–336.
86. Benjamin M, Redman S, Milz S, et al. Adipose tissue at entheses: the rheumatological implications of its distribution. A potential site of pain and stress dissipation? *Ann Rheum Dis* 2004;63:1549–1555.
87. Jarvinen M, Jozsa L, Kannus P, Jarvinen TL, Kvist M, Leadbetter W. Histopathological findings in chronic tendon disorders. *Scand J Med Sci Sports* 1997;7:86–95.
88. Benjamin M, McGonagle D. The enthesis organ concept and its relevance to the spondyloarthropathies. *Adv Exp Med Biol* 2009;649:57–70.
89. Benjamin M, Milz S, Bydder GM. Magnetic resonance imaging of entheses. Part 2. *Clin Radiol* 2008;63:704–711.
90. Peto S, Gillis P, Henri VP. Structure and dynamics of water in tendon from NMR relaxation measurements. *Biophys J* 1990;57:71–84.
91. Juras V, Apprich S, Szomolanyi P, Bieri O, Deligianni X, Trattng S. Bi-exponential T2 analysis of healthy and diseased Achilles tendons: an in vivo preliminary magnetic resonance study and correlation with clinical score. *Eur Radiol* 2013;23:2814–2822.
92. Bogduk N, Endres SM. Clinical anatomy of the lumbar spine and sacrum. New York: Elsevier/Churchill Livingstone; 2005.
93. Cassidy JJ, Hiltner A, Baer E. Hierarchical structure of the intervertebral disc. *Connect Tissue Res* 1989;23:75–88.
94. Levangie PK, Norkin CC. Joint structure and function: a comprehensive analysis. Philadelphia: F.A. Davis; 2005.
95. Roberts S, Urban JP, Evans H, Eisenstein SM. Transport properties of the human cartilage endplate in relation to its composition and calcification. *Spine (Phila Pa 1976)* 1996;21:415–420.
96. Nightingale T, MacKay A, Pearce RH, Whittall KP, Flak B. A model of unloaded human intervertebral disk based on NMR relaxation. *Magn Reson Med* 2000;43:34–44.
97. Bae WC, Stature S, Zhang Z, et al. Morphology of the cartilaginous endplates in human intervertebral disks with ultrashort echo time MR imaging. *Radiology* 2013;266:564–574.
98. Robson MD, Gatehouse PD, Bydder M, Bydder GM. Magnetic resonance: an introduction to ultrashort TE (UTE) imaging. *J Comput Assist Tomogr* 2003;27:825–846.
99. Gold GE, Pauly JM, Macovski A, Herfkens RJ. MR spectroscopic imaging of collagen: tendons and knee menisci. *Magn Reson Med* 1995;34:647–654.
100. Chang EY, Bae WC, Stature S, Du J, Chung CB. Effects of repetitive freeze-thawing cycles on T2 and T2 of the Achilles tendon. *Eur J Radiol* 2014;83:349–353.